

# Electrochemical determination of rutin by using NiFe<sub>2</sub>O<sub>4</sub> nanoparticles loaded reduced graphene oxide

**Nahid Askari**

Kerman Graduate University of Technology: Graduate University of Advanced Technology

**Navvabeh Salarizadeh**

Tehran University: University of Tehran

**Mohammad Bagher Askari** (✉ [nima947@gmail.com](mailto:nima947@gmail.com))

University of Guilan <https://orcid.org/0000-0003-2094-6234>

---

## Research Article

**Keywords:** Rutin, NiFe<sub>2</sub>O<sub>4</sub>, Reduced graphene oxide, electrochemical sensors

**Posted Date:** February 23rd, 2021

**DOI:** <https://doi.org/10.21203/rs.3.rs-172648/v1>

**License:**  This work is licensed under a Creative Commons Attribution 4.0 International License.

[Read Full License](#)

---

**Version of Record:** A version of this preprint was published at Journal of Materials Science: Materials in Electronics on March 12th, 2021. See the published version at <https://doi.org/10.1007/s10854-021-05636-9>.

# Abstract

A binary transition metal oxide based on nickel and iron ( $\text{NiFe}_2\text{O}_4$ ) and hybridization of this nanomaterial with reduced graphene oxide (rGO) are synthesized by the hydrothermal method. X-ray diffraction (XRD), and Raman spectroscopy confirm the successful synthesis of these materials. Also, scanning electron microscope (SEM) and transmission electron microscope (TEM) images illustrated the particle morphology with the particle size of 20 nm. The synthesized material is then examined as a sensor on the surface of the glassy carbon electrode to detect a very small amount of rutin. Some electrochemical tests such as cyclic voltammetry, differential pulse voltammetry, impedance spectroscopy indicate the remarkable accuracy of this sensor and its operation in a relatively wide range of concentration of rutin (100 nM-100  $\mu\text{M}$ ). Considering the very good results, it seems the  $\text{NiFe}_2\text{O}_4$ -rGO can be considered as a new proposal in the development of accurate and inexpensive electrochemical sensors.

## 1 Introduction

The extensive use of rutin in clinical treatments has been received much attention [1, 2]. Rutin has antibacterial [3], antiviral [4], anti-tumor [5], and anti-inflammatory [6] properties. Furthermore, it has effective physiological functions and it has an effective role in diluting the blood [7] and lowering blood pressure [8]. Recently, in some countries, this drug has been included in the coronavirus treatment protocol in the current pandemic [9]. Therefore, the detection of rutin with a simple, rapid, and low-cost sensing method seems necessary.

So far, various methods such as capillary electrophoresis [10], chemiluminescence [11], sequential injection analysis [12], and electrochemical techniques have been used to determine the exact amount of rutin. But among them, the use of electrochemical techniques and the design of a sensor with an electrochemical approach is recommended due to its speed, accuracy, and very low cost [13, 14]. A review of scientific reports indicates different electrochemical sensors with accurate have been considered by the detection of rutin. In the structure of these sensors, precious and rare metals such as platinum, palladium, etc. have been used. Their disadvantage, in addition to high cost, is the complex electrochemical mechanisms in the detection of rutin. Other problems are the very rapid oxidation of these materials and their failure and saturation after several times of detection [15-17].

The design and manufacture of sensors with low cost, high stability, and good anti-interference capability for rutin detection are very significant today. Binary transition metal oxides (BTMO) such as  $\text{NiCo}_2\text{O}_4$  [13],  $\text{CoFe}_2\text{O}_4$  [7],  $\text{ZnFe}_2\text{O}_4$  [18], etc. in the form of  $\text{AB}_2\text{O}_4$  are very popular in electrochemistry. For example, there are many reports on applications in supercapacitor electrodes, hydrogen evolution reaction [19], methanol oxidation [20], urea oxidation [21], supercapacitor [22], etc. In most of the mentioned applications, the good reason for the efficiency of these materials is the synergistic effect between two metal oxides. At the same time, these amazing materials have a very important problem, which is their very low electrical conductivity [23].

Nickel and iron have always been considered as two inexpensive and environmentally friendly elements in electrochemical applications [24-26]. It is clear that a suitable electrode for accurate detection of various drugs, in addition to a high surface area, must also have a very good conductivity but, BTMOs do not have this advantage [27, 28]. Today, the use of carbonaceous materials such as reduced graphene oxides is very popular due to the high surface area and very good conductivity of these materials [29, 30].

In this research, a BTMO nanoparticle,  $\text{NiFe}_2\text{O}_4$ , is synthesized, and to increase its specific surface area and conductivity, it is hybridized with reduced graphene oxide. The synergistic effect between the two metal oxides and rGO shows the good in-vitro results of the detection of rutin in the range of 0.01-00  $\mu\text{M}$  by  $\text{NiFe}_2\text{O}_4$ -rGO. The result confirms the widespread use of BTMOs hybridized with rGO as a biosensor in the field of bioelectrochemistry.

## 2 Experimental

### 2.1 Synthesis of $\text{NiFe}_2\text{O}_4$ and $\text{NiFe}_2\text{O}_4$ -rGO

After synthesizing graphene oxide by Hummers' method [31],  $\text{NiFe}_2\text{O}_4$  and  $\text{NiFe}_2\text{O}_4$ -rGO were synthesized by an easy hydrothermal method. The synthesis method is as following: 2.5 mmol nickel chloride ( $\text{NiCl}_2 \cdot 6\text{H}_2\text{O}$ ) and 5 mmol iron (III) chloride ( $\text{FeCl}_3 \cdot 6\text{H}_2\text{O}$ ) were dissolved in 50 ml deionized water and stirred for 10 minutes by sonicating, and then 20 mmol sodium acetate ( $\text{CH}_3\text{COONa}$ ) added in the above solution and stirred for 30 minutes. The solution was injected into the 100 ml stainless steel reactor, and the reaction continued in the oven at 180 °C for 24 hours. After that, the resulting material was washed with deionized water and ethanol several times, and calcinate at a temperature of 300 °C for 2 hours. The resulting powder is  $\text{NiFe}_2\text{O}_4$ .

The synthesis of the  $\text{NiFe}_2\text{O}_4$ -rGO was performed with the same method, with the difference that at the first, a certain amount of GO was added to the mentioned nickel and iron sources. XRD, and Raman spectroscopy analysis were performed to confirm the synthesis of  $\text{NiFe}_2\text{O}_4$  and  $\text{NiFe}_2\text{O}_4$ -rGO. Also, the morphology and the size of these materials were examined with scanning electron microscopy (SEM) and transmission electron microscopy (TEM).

### 2.2 Material characterization

The XRD analysis of rGO,  $\text{NiFe}_2\text{O}_4$ , and  $\text{NiFe}_2\text{O}_4$ -rGO were conducted BY XRD 3000 EQUINOX INEL with CuK $\alpha$  lamp to confirm the synthesis and study the crystal structure. As predicted, in Figure 1 the presence of two relatively wide peaks at angles of about 25° and 43° confirms the successful synthesis of rGO. In the 2 $\theta$  of 18.4°, 30.3°, 35.7°, 43.2°, 53.8°, 57.4°, 63.2°, and 74.6° there are characteristic peaks that belong to (111), (220), (311), (400), (422), (511), (440), and (533) planes, respectively, which confirm the successful synthesis of  $\text{NiFe}_2\text{O}_4$  that is in full compliance with JCPDS (Card No. 10-0325) [32]. Using the Scherrer equation

$$(t = \frac{0.9\lambda}{\beta \cos \theta}),$$

the size of nanoparticles is estimated to be about 20 nm, which is also consistent with the TEM results. What is clear and seen in similar works, in most cases with the combination of nanoparticles and graphene, the amount of crystallinity is reduced. Figure 1 shows some NiFe<sub>2</sub>O<sub>4</sub> peaks disappear when it hybridized with rGO, and others peaks slightly shifted by overlapping with rGO characteristic peaks [33].

One of the most important analyses that are always important for carbon composites is Raman spectroscopy. Raman spectra were collected with Thermo Nicolet Almega XR Raman. Figure 2 shows the Raman spectrum of rGO with two peaks at 1594 and 1354 cm<sup>-1</sup>, known as the D-band and the G-band, respectively. The D and G bands belong to the defects and sp<sup>3</sup> carbon, respectively. In the NiFe<sub>2</sub>O<sub>4</sub>-rGO spectrum (Figure 2), two peaks are specified in the Eg vibration states at 336 and 666 cm<sup>-1</sup>. Also, the T<sub>2g</sub> vibration mode is specified at 497 cm<sup>-1</sup>. In addition to the aforementioned peaks, the A<sub>1g</sub> vibration mode has also appeared at 574 and 706 cm<sup>-1</sup>. The compatibility of the peaks shown in NiFe<sub>2</sub>O<sub>4</sub> with other studies confirms its successful synthesis [32, 34].

SEM images related to rGO, NiFe<sub>2</sub>O<sub>4</sub>, and NiFe<sub>2</sub>O<sub>4</sub>-rGO are shown in Figures 3a-c, respectively. These images were prepared to study the morphology and size of the synthesized nanomaterials. As can be seen in Figure 3a, graphene nanosheets have a clear two-dimensional morphology. Figure 3b shows the spherical morphology of NiFe<sub>2</sub>O<sub>4</sub> nanoparticles. In Figure 3c, these nanoparticles are uniformly placed on the surface of rGO plates.

To prove this uniform dispersion, the Energy dispersive X-ray (EDX) mapping analysis was done and the results are shown in Figure 3d. EDX mapping images confirm the uniform dispersion of NiFe<sub>2</sub>O<sub>4</sub> nanoparticles on the surface of rGO and also approve the presence of nickel, iron, oxygen, and carbon in the structure of this nanohybrid.

The specific surface area and porosity are very important features of hybrid composites for biosensor applications. In this study, the surface of nanomaterials was calculated by the Brunauer-Emmett-Teller (BET) surface area analysis (Figure 3e). Increasing the surface area increases the active sites in the nanomaterials and makes redox reactions easier. Adding rGO to NiFe<sub>2</sub>O<sub>4</sub> increases the surface area of NiFe<sub>2</sub>O<sub>4</sub>-rGO to 187.2 m<sup>2</sup> g<sup>-1</sup>. Also, the BET specific surface area is 91 m<sup>2</sup> g<sup>-1</sup> for rGO and 111 m<sup>2</sup> g<sup>-1</sup> for NiFe<sub>2</sub>O<sub>4</sub>.

Figures 4a-c indicate the TEM images of rGO, NiFe<sub>2</sub>O<sub>4</sub>, and NiFe<sub>2</sub>O<sub>4</sub>-rGO, respectively. As can be seen in Figure 4a, transparent graphene sheets are very thin and also indicate the few layers. Figure 4b shows the TEM image of NiFe<sub>2</sub>O<sub>4</sub> nanoparticles. The particle size in this image is about 20 nm, which is compatible with the XRD results. Figure 4c also shows the uniform placement of the NiFe<sub>2</sub>O<sub>4</sub> nanoparticles on the

surface of transparent rGO plates. The incorporating of NiFe<sub>2</sub>O<sub>4</sub> in rGO can provide active sites, increase the dispersion of nanoparticles, and prevents agglomeration.

### 3 Electrochemical Characterizations

0.01 g of each of NiFe<sub>2</sub>O<sub>4</sub> and NiFe<sub>2</sub>O<sub>4</sub>-rGO was dissolved by sonication in a solution of Nafion and isopropyl alcohol/water (70:30) for 20 minutes. Then, 10  $\mu$ L of the resulting slurry (equivalent to one drop) was placed on the surface of a glassy carbon electrode (GCE) and dried at room temperature. The GCE electrode modified by each of the NiFe<sub>2</sub>O<sub>4</sub> and NiFe<sub>2</sub>O<sub>4</sub>-rGO nanomaterials will act as the working electrode. Ag/AgCl and platinum wire (0.5 mm diameter) was used as the reference and auxiliary electrodes, respectively. The modified electrode was dried for 1 hour at 40 °C, and the sensitivity of the nanomaterials examined to rutin detection.

As mentioned, one of the most important reasons for adding rGO to the NiFe<sub>2</sub>O<sub>4</sub> structure was to increase the conductivity as well as the effective surface area. The increase in the active surface area, as shown in the BET, was achieved by adding rGO. Figure 5a shows cyclic voltammetry of NiFe<sub>2</sub>O<sub>4</sub> and NiFe<sub>2</sub>O<sub>4</sub>-rGO in 0.1 M KOH solution at the potential range of 0 to 500 mV. A redox peak in both diagrams is indicated. Increasing the current density as well as decreasing the overpotential in the graphene-containing electrode confirms the increase in electrode conductivity by adding rGO to the structure of NiFe<sub>2</sub>O<sub>4</sub>.

Impedance analysis was also performed on the electrodes containing rGO and without it. In this analysis, the semicircle diameter indicates Rct, which represents the resistance to the charge transfer. As shown in Figure 5b, the Rct in NiFe<sub>2</sub>O<sub>4</sub>-rGO is 65  $\Omega$  and in NiFe<sub>2</sub>O<sub>4</sub> is 116  $\Omega$ , showing increasing of conductivity by adding rGO to the NiFe<sub>2</sub>O<sub>4</sub>. Thus, NiFe<sub>2</sub>O<sub>4</sub>-rGO/GCE electrode was selected as the working electrode and other rutin detection tests were performed with this electrode.

#### 3.1 Effect of pH in rutin detection

To investigate the mechanism of rutin electro-oxidation, CV analysis in different pHs was performed at PBS 0.1 M in a scan rate of 20 mV/s. As shown in Figure 6a, the anodic peak current of rutin oxidation (I<sub>pa</sub>) has increased when pH changed from 1 to 2, and the increase in I<sub>pa</sub> from pH = 2 to 3 is relatively high significant. The current density at pH=3 reaches the maximum value, then the current density gradually decreases with increasing pH value from 3 to 6. Then, by selecting pH=3, as the most suitable pH, the sensitivity of the proposed sensor for very low concentrations and also the effect of scan rate on the rutin electro-oxidation process will be investigated. At low pHs, the peak current increases due to the electrostatic interactions between the negative charge of the NiFe<sub>2</sub>O<sub>4</sub>/rGO and the positive charge of rutin. At high pHs, the degree of protonation of rutin reduces resulting in less interaction between electrode and analyte.

#### 3.2 Effect of scan rate on rutin detection

To investigate the effect of the scan rate on the rutin oxidation process, the CV test of NiFe<sub>2</sub>O<sub>4</sub>-rGO/GCE electrode was performed at different scan rates (20 to 200 mV/s) in 0.1 M PBS (pH = 3) and 1 μM rutin. As shown in Figure 6a, redox peaks become sharper as the scan rate increases. With increasing in scan rate, the peak potential tends to positive values, indicating that the reaction is quasi-reversible. As we know, I<sub>pa</sub> and I<sub>pc</sub> are the maximum current density at the forward and backward scan, respectively. Figure 6b shows that I<sub>pa</sub> and I<sub>pc</sub> are simultaneously increasing with the increase in the scan rate. By drawing of the log I<sub>pa</sub> during oxidation as well as the log I<sub>pc</sub> during a reduction according to log v, two equations are obtained from the following equations.

$$\text{Log } I_{pa} = -0.34 + 0.84 \log v \quad (1)$$

$$\text{Log } I_{pc} = 0.44 - 0.84 \log v \quad (2)$$

The logarithmic diagram of I<sub>pa</sub> and I<sub>pc</sub> according to the logarithm v shown in Figure 6c. This diagram shows the linear relationship between log I<sub>pa</sub> and log v with R<sup>2</sup> = 0.982 and log I<sub>pc</sub> with log v with R<sup>2</sup> = 0.981. As is clear, the slope is between 0.5 and 1, representing that both diffusion and adsorption processes simultaneously control the electrochemical reactions. In Figure 6d, the I<sub>pa</sub> and I<sub>pc</sub> diagrams are plotted in terms of a square root of the scan rate (v<sup>1/2</sup>). The calculation of the regression line for I<sub>pa</sub> and I<sub>pc</sub> show R<sup>2</sup> = 0.917, indicating the diffusion-controlled process is dominant in the rutin detection.

### 3.3 Quantitative analysis of rutin by DPV

To evaluate the sensitivity of NiFe<sub>2</sub>O<sub>4</sub>-rGO electrode for measuring very small amounts of rutin, differential pulse voltammetry (DPV) analysis was performed in 0.1 M PBS, (pH=3) and the concentration range of 100 μM to 100 nM rutin (Figure 7a). As it is clear, I<sub>pa</sub> decreases with decreasing rutin concentration, and finally reaches a minimum at a concentration of 100 nM, and there is almost no current at concentrations below 100 nM. In general, it can be said that the detection limit of the proposed sensor is 100 nM rutin, which is almost a competitive and appropriate value compared to previous works [13, 35-39]. This good sensitivity results can be related to the synergistic effect between rGO and NiFe<sub>2</sub>O<sub>4</sub> nanoparticles. Drawing I<sub>pa</sub> graph according to rutin concentration and obtaining the equation with regression R<sup>2</sup>=0.99 indicates the linearity of the relationship and the satisfactory results (Figure 7b). Also, to evaluate the stability of this proposed electrochemical sensor, DPV analysis was performed for 100 times at a rutin concentration of 100 nM in 0.1 M PBS, (pH=3). The results show that I<sub>pa</sub> decreases less than 5% after 100<sup>th</sup> (Figure 7c), which confirms the relatively good stability of the proposed sensor.

According to previous researches, the mechanism of rutin oxidation is containing two-electron/two-proton oxidation process, which takes place in several stages [36]. The mechanism is shown in Figure 8. At the first, a phenoxy radical (the most stable form is shown in Figure 9) is created by electron transfer, and then a carbocation creates during a second electron transfer. After that, 3',4'-diquinone is obtained by dehydration of the carbocation and then it reduced to rutin during the reverse reaction.

## 4 Conclusion

BTMOs are very popular in electrochemical applications. In this study, a NiFe<sub>2</sub>O<sub>4</sub> and NiFe<sub>2</sub>O<sub>4</sub>-rGO were synthesized. XRD, Raman, SEM, TEM, and BET confirmed the successful synthesis of NiFe<sub>2</sub>O<sub>4</sub> nanoparticles. The electrochemical investigations proved the NiFe<sub>2</sub>O<sub>4</sub>-rGO electrode has advantages compared to the NiFe<sub>2</sub>O<sub>4</sub> electrode in terms of conductivity and sensitivity. NiFe<sub>2</sub>O<sub>4</sub>-rGO electrode can be detected at very low concentrations of rutin (100 nM). Thus, this electrode can be proposed as a sensitive and stable option for rutin detection.

## References

1. Gul, A., et al., *Rutin and rutin-conjugated gold nanoparticles ameliorate collagen-induced arthritis in rats through inhibition of NF- $\kappa$ B and iNOS activation*. International immunopharmacology, 2018. **59**: p. 310-317.
2. Hou, L.-S., et al., *Rutin mitigates hepatic fibrogenesis and inflammation through targeting TLR4 and P2X7 receptor signaling pathway in vitro and in vivo*. Journal of Functional Foods, 2020. **64**: p. 103700.
3. Deepika, M.S., et al., *Antibacterial synergy between rutin and florfenicol enhances therapeutic spectrum against drug resistant Aeromonas hydrophila*. Microbial pathogenesis, 2019. **135**: p. 103612.
4. Alam, P., et al., *Quantitative analysis of rutin, quercetin, naringenin, and gallic acid by validated RP- and NP-HPTLC methods for quality control of anti-HBV active extract of Guiera senegalensis*. Pharmaceutical Biology, 2017. **55**(1): p. 1317-1323.
5. Allgäuer, M., et al., *Implementing tumor mutational burden (TMB) analysis in routine diagnostics—a primer for molecular pathologists and clinicians*. Translational lung cancer research, 2018. **7**(6): p. 703.
6. Gene, R.M., et al., *Anti-inflammatory and analgesic activity of Baccharis trimera: identification of its active constituents*. Planta medica, 1996. **62**: p. 232-235.
7. Ansari, S.H. and M. Arvand, *A magnetic nanocomposite prepared from electrospun CoFe<sub>2</sub>O<sub>4</sub> nanofibers and graphene oxide as a material for highly sensitive determination of rutin*. Microchimica Acta, 2020. **187**(2): p. 1-9.
8. Oyagbemi, A.A., et al., *Ameliorative effect of Rutin on sodium fluoride-induced hypertension through modulation of Kim-1/NF- $\kappa$ B/Nrf2 signaling pathway in rats*. Environmental toxicology, 2018. **33**(12): p. 1284-1297.
9. Yang, R., et al., *Chemical composition and pharmacological mechanism of Qingfei Paidu Decoction and Ma Xing Shi Gan Decoction against Coronavirus Disease 2019 (COVID-19): in silico and experimental study*. Pharmacological Research, 2020: p. 104820.
10. Wagner, F.F., et al., *Extended donor typing by pooled capillary electrophoresis: impact in a routine setting*. Transfusion Medicine and Hemotherapy, 2018. **45**(4): p. 225-237.

11. Tan, H., et al., *A covalent triazine framework as an oxidase mimetic in the luminol chemiluminescence system: application to the determination of the antioxidant rutin*. *Microchimica Acta*, 2020. **187**(1): p. 42.
12. Miekh, Y.V., et al., *Simultaneous determination of rutin and ascorbic acid in a sequential injection lab-at-valve system*. *Journal of Pharmaceutical and Biomedical Analysis*, 2018. **149**: p. 179-184.
13. Cui, S., et al., *Mesoporous NiCo<sub>2</sub>O<sub>4</sub>-decorated reduced graphene oxide as a novel platform for electrochemical determination of rutin*. *Talanta*, 2017. **164**: p. 291-299.
14. He, Q., et al., *Facile electrochemical sensor for nanomolar rutin detection based on magnetite nanoparticles and reduced graphene oxide decorated electrode*. *Nanomaterials*, 2019. **9**(1): p. 115.
15. Li, S., et al., *Nonenzymatic electrochemical detection of rutin on Pt nanoparticles/graphene nanocomposite modified glassy carbon electrode*. *Analytical Methods*, 2016. **8**(27): p. 5435-5440.
16. Liu, C., J. Huang, and L. Wang, *Electrochemical synthesis of a nanocomposite consisting of carboxy-modified multi-walled carbon nanotubes, polythionine and platinum nanoparticles for simultaneous voltammetric determination of myricetin and rutin*. *Microchimica Acta*, 2018. **185**(9): p. 414.
17. Liu, Z., Q. Xue, and Y. Guo, *Sensitive electrochemical detection of rutin and isoquercitrin based on SH- $\beta$ -cyclodextrin functionalized graphene-palladium nanoparticles*. *Biosensors and Bioelectronics*, 2017. **89**: p. 444-452.
18. Ghoreishi, S.M. and M. Malekian, *Curve resolution on overlapped voltammograms for simultaneous determination of tryptophan and tyrosine at carbon paste electrode modified with ZnFe<sub>2</sub>O<sub>4</sub> nanoparticles*. *Journal of Electroanalytical Chemistry*, 2017. **805**: p. 1-10.
19. Li, S., et al., *Doping  $\beta$ -CoMoO<sub>4</sub> nanoplates with phosphorus for efficient hydrogen evolution reaction in alkaline media*. *ACS applied materials & interfaces*, 2018. **10**(43): p. 37038-37045.
20. Askari, M.B., P. Salarizadeh, and A. Beheshti-Marnani, *A hierarchical hybrid of ZnCo<sub>2</sub>O<sub>4</sub> and rGO as a significant electrocatalyst for methanol oxidation reaction: Synthesis, characterization, and electrocatalytic performance*. *International Journal of Energy Research*.
21. Babar, P., et al., *Bifunctional 2D electrocatalysts of transition metal hydroxide nanosheet arrays for water splitting and urea electrolysis*. *ACS Sustainable Chemistry & Engineering*, 2019. **7**(11): p. 10035-10043.
22. Askari, M.B. and P. Salarizadeh, *Binary nickel ferrite oxide (NiFe<sub>2</sub>O<sub>4</sub>) nanoparticles coated on reduced graphene oxide as stable and high-performance asymmetric supercapacitor electrode material*. *International Journal of Hydrogen Energy*, 2020.
23. Salarizadeh, P., et al., *Pristine NiCo<sub>2</sub>O<sub>4</sub> nanorods loaded rGO electrode as a remarkable electrode material for asymmetric supercapacitors*. *Materials Science in Semiconductor Processing*, 2020. **114**: p. 105078.
24. Feng, X., et al., *Construction of hierarchical nickel/cobalt iron-hydroxide and nickel/cobalt selenide nanotubes for efficient electrocatalytic water splitting*. *New Journal of Chemistry*, 2020. **44**(18): p. 7552-7560.

25. Wang, Y., et al., *Environmentally-Friendly Exfoliate and Active Site Self-Assembly: Thin 2D/2D Heterostructure Amorphous Nickel–Iron Alloy on 2D Materials for Efficient Oxygen Evolution Reaction*. *Small*, 2019. **15**(16): p. 1805435.
26. Yan, B., et al., *Salt Powder Assisted Synthesis of Nanostructured Materials and Their Electrochemical Applications in Energy Storage Devices*. *Chemical Engineering Journal*, 2020: p. 125895.
27. Chan, Y., et al., *Solution-processed wrinkled electrodes enable the development of stretchable electrochemical biosensors*. *Analyst*, 2018. **144**(1): p. 172-179.
28. Mousa, H.M., J.R. Aggas, and A. Guiseppi-Elie, *Electropolymerization of aniline and (N-phenyl-o-phenylenediamine) for glucose biosensor application*. *Materials Letters*, 2019. **238**: p. 267-270.
29. Askari, M.B., et al., *Binary mixed molybdenum cobalt sulfide nanosheets decorated on rGO as a high-performance supercapacitor electrode*. *Nanotechnology*, 2020. **31**(27): p. 275406.
30. Repp, S., et al., *Synergetic effects of Fe 3+ doped spinel Li 4 Ti 5 O 12 nanoparticles on reduced graphene oxide for high surface electrode hybrid supercapacitors*. *Nanoscale*, 2018. **10**(4): p. 1877-1884.
31. Hummers Jr, W.S. and R.E. Offeman, *Preparation of graphitic oxide*. *Journal of the american chemical society*, 1958. **80**(6): p. 1339-1339.
32. Kumar, N., et al., *Facile synthesis of mesoporous NiFe<sub>2</sub>O<sub>4</sub>/CNTs nanocomposite cathode material for high performance asymmetric pseudocapacitors*. *Applied Surface Science*, 2018. **433**: p. 1100-1112.
33. Salarizadeh, P., et al., *Synergistic Effect of MoS<sub>2</sub> and Fe<sub>3</sub>O<sub>4</sub> Decorated Reduced Graphene Oxide as a Ternary Hybrid for High-Performance and Stable Asymmetric Supercapacitors*. *Nanotechnology*.
34. Dunst, K., et al., *Study of the NO<sub>2</sub> sensing mechanism of PEDOT-RGO film using in situ Raman spectroscopy*. *Sensors and Actuators B: Chemical*, 2018. **260**: p. 1025-1033.
35. D'Souza, O.J., et al., *A novel ZnO/reduced graphene oxide and Prussian blue modified carbon paste electrode for the sensitive determination of Rutin*. *Science China Chemistry*, 2019. **62**(2): p. 262-270.
36. El Jaouhari, A., et al., *Enhanced molecular imprinted electrochemical sensor based on zeolitic imidazolate framework/reduced graphene oxide for highly recognition of rutin*. *Analytica Chimica Acta*, 2020. **1106**: p. 103-114.
37. Wang, Z., et al., *One-step synthesis of a methylene blue@ ZIF-8-reduced graphene oxide nanocomposite and its application to electrochemical sensing of rutin*. *Microchimica Acta*, 2018. **185**(5): p. 279.
38. Westland, J.L. and F.L. Dorman, *QuEChERS extraction of benzodiazepines in biological matrices*. *Journal of pharmaceutical analysis*, 2013. **3**(6): p. 509-517.
39. Yalikun, N., et al., *Taraxacum-like Mg-Al-Si@ porous carbon nanoclusters for electrochemical rutin detection*. *Microchimica Acta*, 2019. **186**(6): p. 379.

## Figures

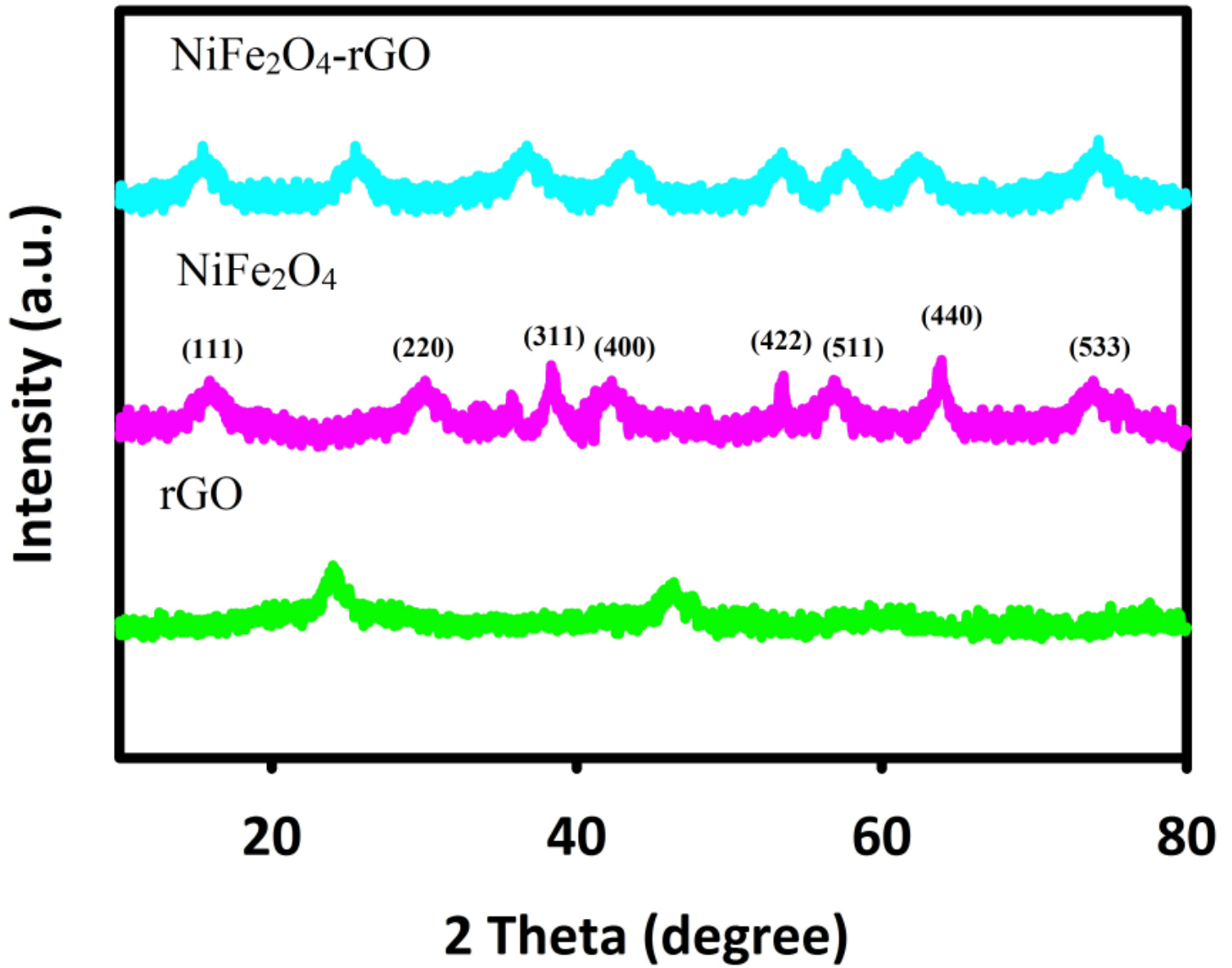


Figure 1

The Raman spectra of rGO, NiFe<sub>2</sub>O<sub>4</sub>, and NiFe<sub>2</sub>O<sub>4</sub>-rGO.

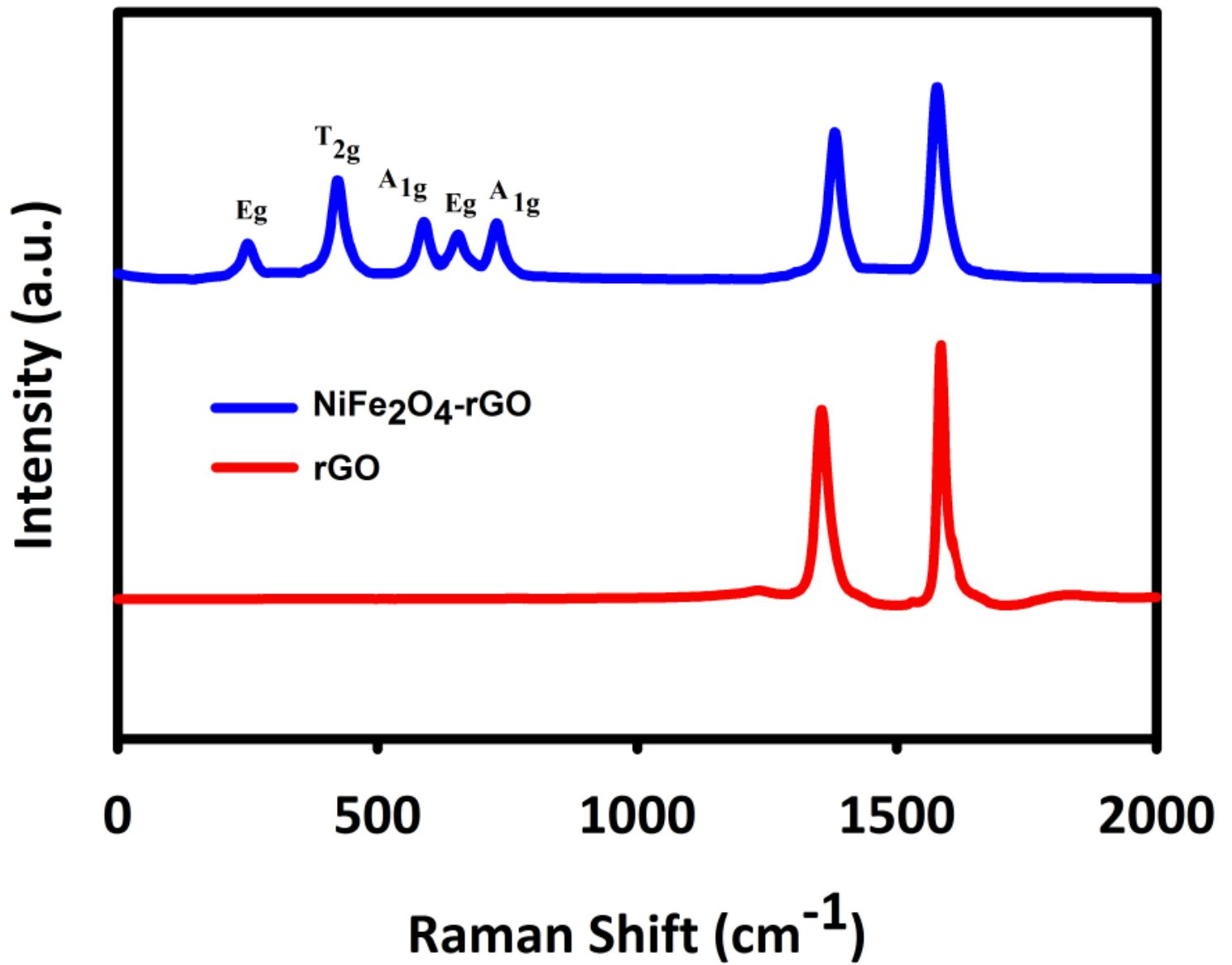
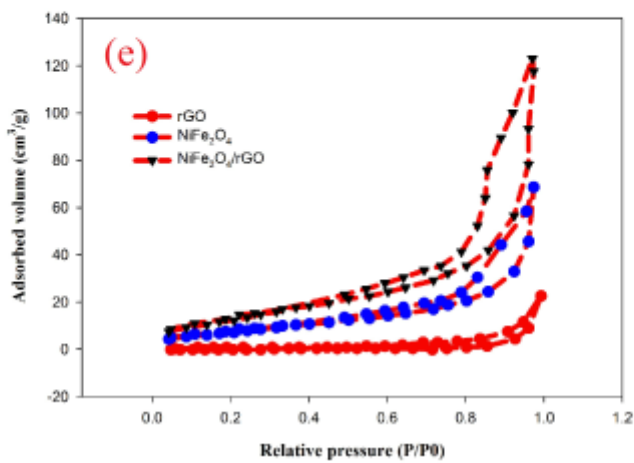
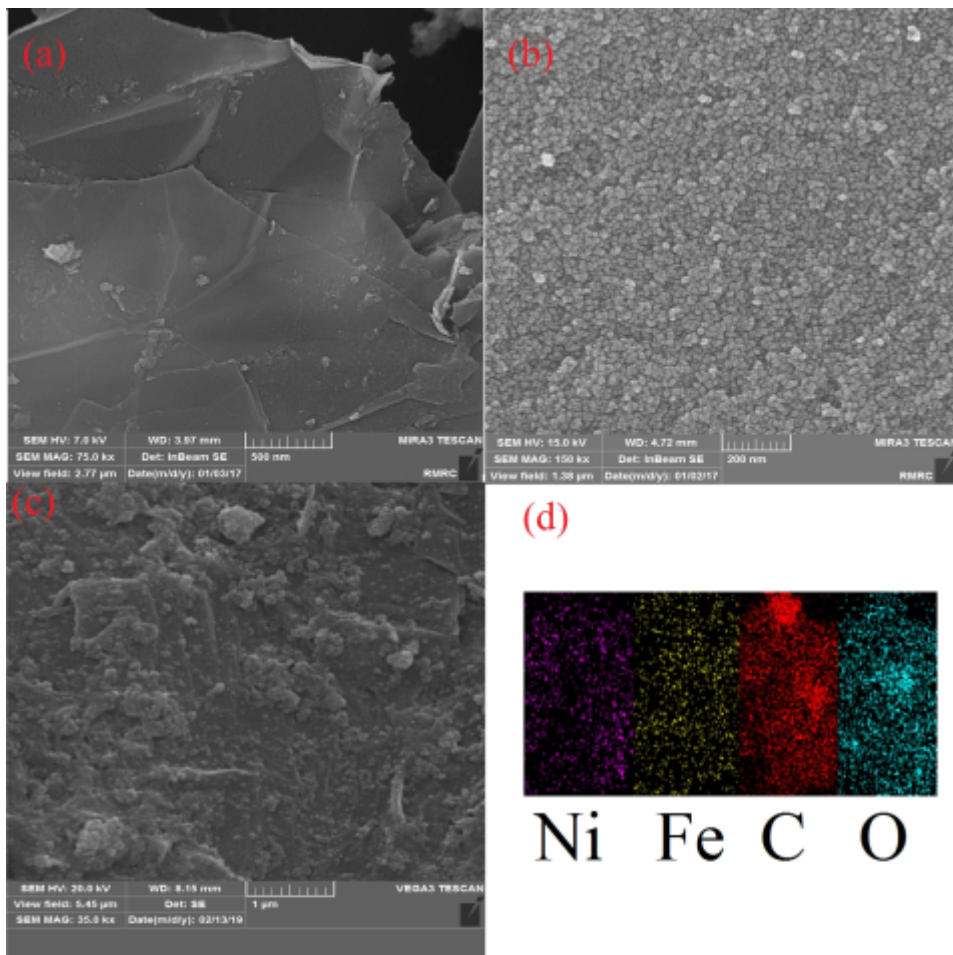


Figure 2

The Raman spectra of rGO and NiFe<sub>2</sub>O<sub>4</sub>.



**Figure 3**

SEM micrographs of rGO (a), NiFe<sub>2</sub>O<sub>4</sub> (b), and NiFe<sub>2</sub>O<sub>4</sub>-rGO (c), EDX mapping of NiFe<sub>2</sub>O<sub>4</sub> (d), and BET of rGO, NiFe<sub>2</sub>O<sub>4</sub>, and NiFe<sub>2</sub>O<sub>4</sub>-rGO (e).

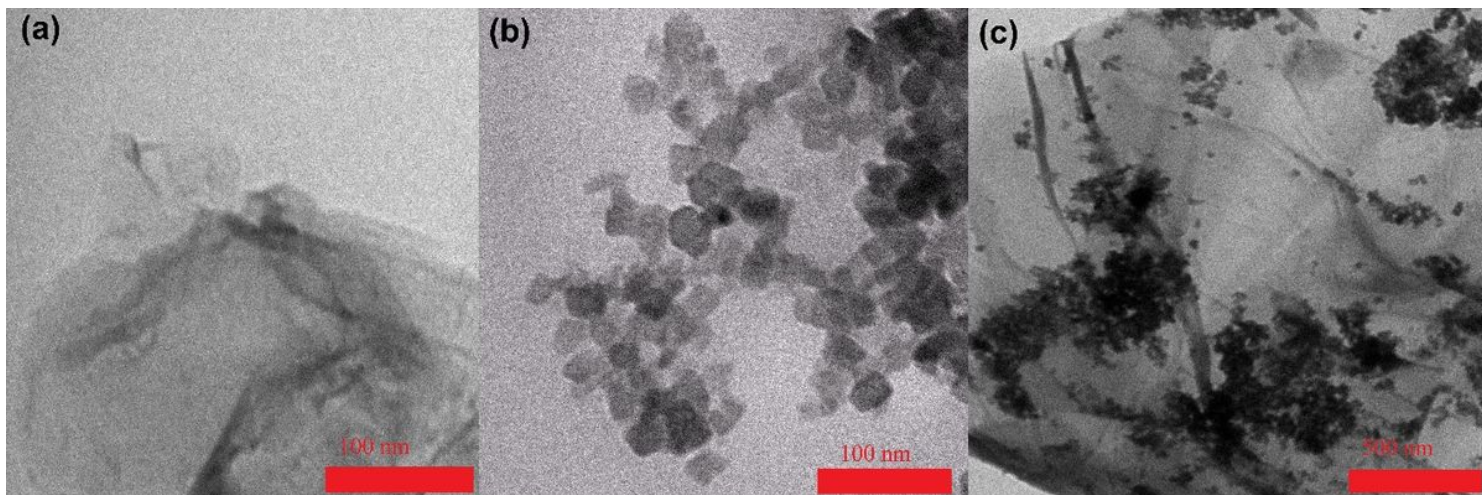


**Figure 4**

The TEM images of rGO (a), NiFe<sub>2</sub>O<sub>4</sub> (b), and NiFe<sub>2</sub>O<sub>4</sub>-rGO (c).

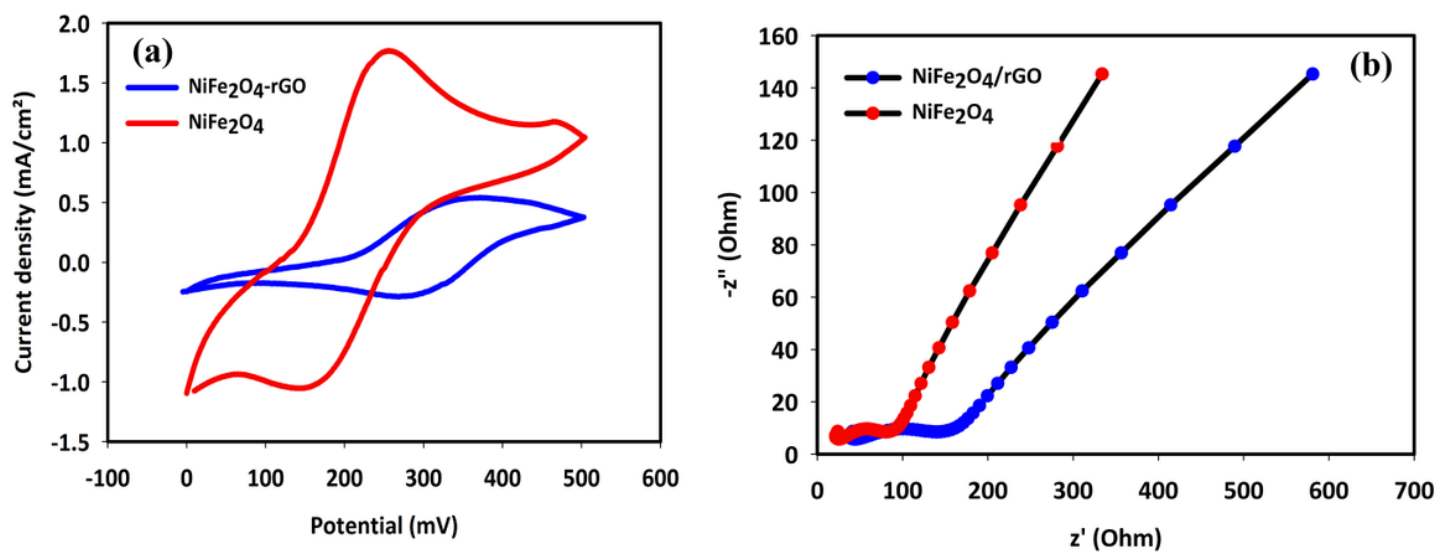


**Figure 5**

CV curves (a) and EIS plots (b) of NiFe<sub>2</sub>O<sub>4</sub> and NiFe<sub>2</sub>O<sub>4</sub>-rGO.

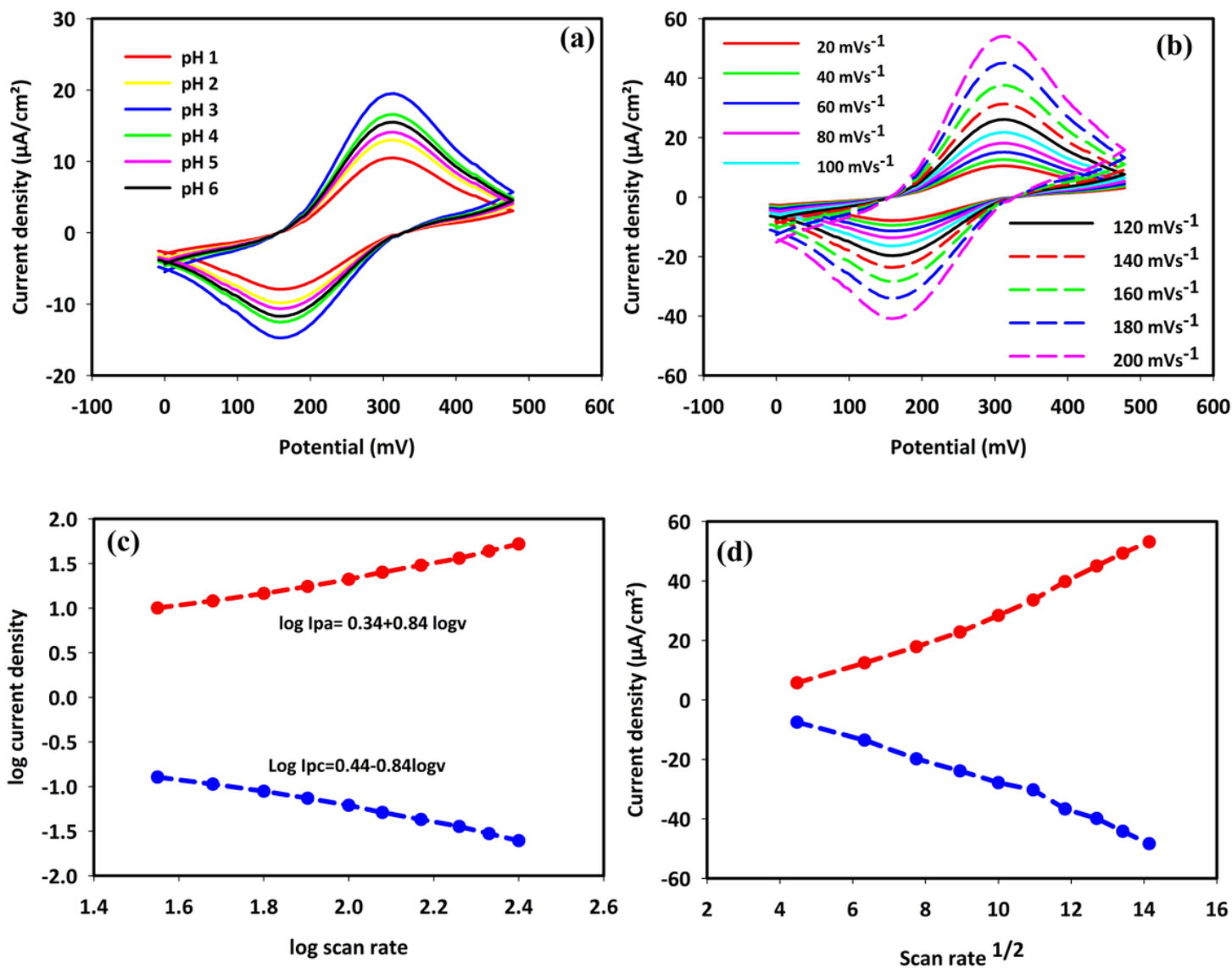
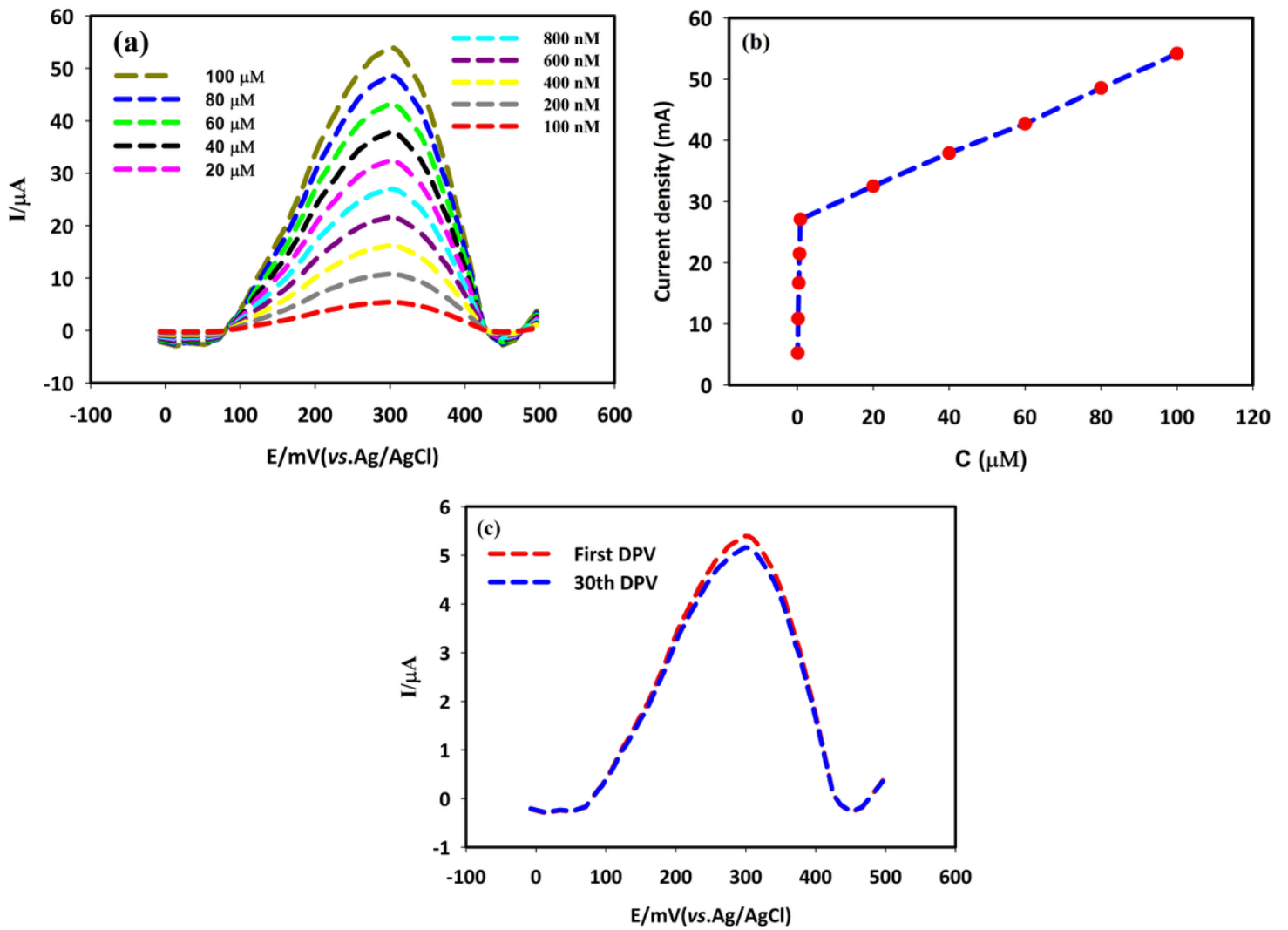


Figure 6

The CV curves of NiFe<sub>2</sub>O<sub>4</sub>-rGO at different pHs (a) and various scan rates (b) and  $\log I_{pa}$  and  $I_{pc}$  versus  $\log$  scan rate (c) and the square root of scan rate (d).



**Figure 7**

DPV curves of NiFe<sub>2</sub>O<sub>4</sub>-rGO at different concentration of rutin (a) the plot of current density versus rutin concentration (b), and DPV curves at first and 30th cycle (c).

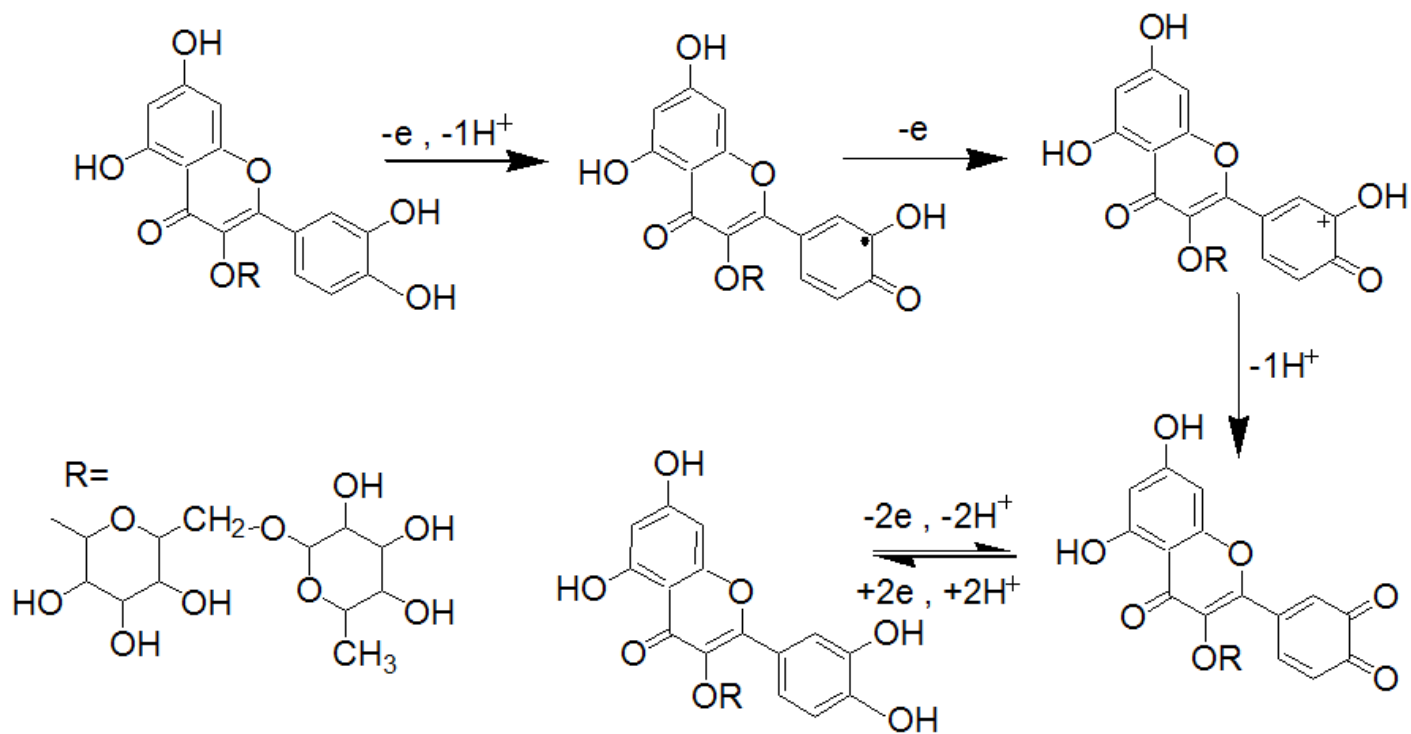


**Figure 8**

Schematic of rutin oxidation.